ACS APPLIED BIO MATERIALS

www.acsabm.org Article

Self-Assembling PCL–PAMAM Linear Dendritic Block Copolymers (LDBCs) for Bioimaging and Phototherapeutic Applications

Indika Chandrasiri, Daniel G. Abebe, Mahesh Loku Yaddehige, Jon Steven Dal Williams, Mohammad Farid Zia, Austin Dorris, Abigail Barker, Briana L. Simms, Azaziah Parker, Bhavani Prasad Vinjamuri, Ngoc Le, Jacqueline N. Gayton, Mahavir Bhupal Chougule, Nathan I. Hammer, Alex Flynt, Jared H. Delcamp, and Davita L. Watkins*

Cite This: *ACS Appl. Bio Mater.* 2020, 3, 5664–5677 Read Online

ACCESS | Metrics & More | Article Recommendations | Supporting Information

ABSTRACT: This study represents a successful approach toward employing polycaprolactone–polyamidoamine (PCL–PAMAM) linear dendritic block copolymer (LDBC) nanoparticles as small-molecule carriers in NIR imaging and photothermal therapy. A feasible and robust synthetic strategy was used to synthesize a library of amphiphilic LDBCs with well-controlled hydrophobic-to-hydrophilic weight ratios. Systems with a hydrophobic weight ratio higher than 70% formed nanoparticles in aqueous media, which show hydrodynamic diameters of 51.6 and 96.4 nm. These nanoparticles exhibited loading efficiencies up to 21% for a hydrophobic molecule and 64% for a hydrophilic molecule. Furthermore, successful cellular uptake was observed via trafficking into endosomal and lysosomal compartments with an encapsulated NIR theranostic agent (C3) without inducing cell death. A preliminary photothermal assessment resulted in cell death after treating the cells with encapsulated C3 and exposing them to NIR light. The results of this work confirm the potential of these polymeric materials as promising candidates in theranostic nanomedicine.

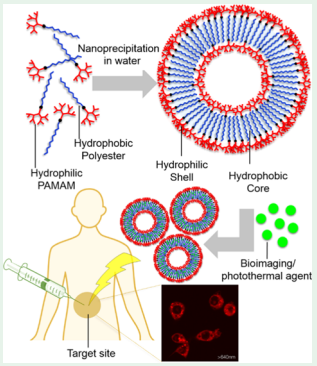

KEYWORDS: *nanocarriers, block copolymers, photothermal therapy, NIR imaging, theranostics, self-assembly, nanoaggregates, nanoparticles*

INTRODUCTION

Modern advances in nanotechnology have opened the doors to the enhancement of distinctively novel aspects of nanomedicine. Applications such as drug delivery, therapy, *in vivo* imaging, and *in vitro* diagnostics are the aspects of nanomedicine that have attracted close attention in health care. Such applications are advantageous in cancer treatment over conventional chemotherapeutic approaches as they enable target-specific delivery, as well as simultaneous delivery of multiple therapeutic agents. Other advantages include the utilization of specific binding moieties to target cancer cells and simultaneous visualization of tumors using an encapsulated imaging agent. All of these benefits have widened the boundaries of nanomedicine toward theranostics.[1−5] However, an applicational drawback is the high hydrophobicity of many commonly used chemotherapeutic agents (e.g., taxanes) and the use of synthetic solvents (e.g., polysorbate 80), which increase the solubility of those therapeutic agents in body fluid, yet are well-known to induce adverse side effects.[6,7]

Increasing interest has been focused on the potential of polymeric nanoparticles (PNs) to revolutionize modern nanomedicine. Among those PNs, polymeric micelles (PMs) and polymersomes are the most extensively studied systems due to their remarkable therapeutic potential.[8−12] PMs can be formed through the self-assembly of amphiphilic block copolymers (BCPs). When these BCPs are introduced to an aqueous environment, they spontaneously assemble into core–shell micellar structures to decrease the free energy of the system.[13−15] This micellar morphology provides an optimal drug delivery system for therapeutic agents. The hydrophobic core is capable of carrying hydrophobic molecules with high loading capacity, and the hydrophilic shell enhances the stability of the nanocarrier in the blood by providing steric protection. PMs possess relatively low critical aggregation concentration (CAC) values that lead to enhanced stability in blood when compared to liposomes and other surfactant micelles.[3,16] In addition, PMs are considerably larger, thus allowing the transfer of more therapeutic agents than other polymer–drug conjugates and have the ability to release the drug in a more controlled manner.[3,17−21]

However, research has shown that *in vivo* applications of conventional micelles fail to provide their projected efficacy, mainly due to premature disintegration during circulation.[3,16]

Received: April 18, 2020
Accepted: July 27, 2020
Published: July 27, 2020

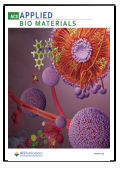

https://dx.doi.org/10.1021/acsabm.0c00432
ACS Appl. Bio Mater. 2020, 3, 5664–5677

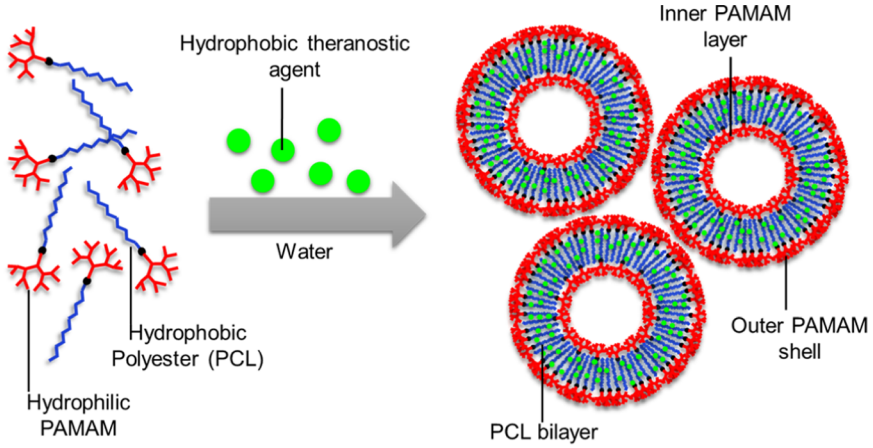

Figure 1. Graphical representation of PCL-G3 LDBCs forming vesicles in water by nanoprecipitation while encapsulating a hydrophobic imaging/photothermal agent.

On the other hand, polymersomes (polymeric vesicles) made of biodegradable amphiphilic BCPs have shown superior physicochemical properties when compared to PMs. Polymersomes have been shown to exhibit enhanced stability, extended circulation times, and slow release of the therapeutic agent. The reason for this high stability and longer retention time is based on their low CAC values (i.e., relative to PMs) and the slow exchange dynamics of the amphiphilic block copolymers that form the nanoparticle.[22−24] Furthermore, the improved colloidal and mechanical stabilities of these polymersomes make them a better candidate than PMs to be utilized in nanomedicine.[25,26]

In the synthesis of these biocompatible PNs, polylactic-*co*-glycolic acid (PLGA), poly(lactic acid) (PLA), and poly(ethylene glycol) (PEG) are currently employed and have been mostly used in the synthesis of linear BCPs.[12,20] Biocompatible linear dendritic block copolymers (LDBCs), generally referred to as hybrid materials, are a unique type of novel amphiphilic BCPs that have proven to be efficient and highly effective in nanomedicine.[27,28] By combining the desirable properties of both linear and dendritic (i.e., branched) macromolecules, these copolymers produce a composition of segments with unique molecular architectures and exceptional chemical properties. Recently, we reported an accessible and robust synthetic methodology for the preparation of a library of LDBCs.[15] Bilayer vesicles were observed for the systems consisting of hydrophobic portions >50 wt % (CAC <6.59 mg/L) and attracted particular interest due to their biomimetic nature (i.e., resembling biological vesicles). This work has laid the foundation for a diverse library of biocompatible and biodegradable materials, which provides evidence of potential applications in nanomedicine.

Herein, we present a novel library of LDBCs composed of PCL (hydrophobic) and polyamidoamine (PAMAM) (hydrophilic) as PNs for theranostic nanomedicine (Figure 1). A library of 50, 70, and 90 (i.e., weight percentage concerning PCL) LDBCs were synthesized, and their compositions were confirmed. Nanoparticles were then formed in aqueous media by nanoprecipitation, and the resulting structures were studied by dynamic light scattering (DLS) and transmission electron microscopy (TEM). As a proof of concept study in theranostics, the capacity of the NPs to encapsulate hydrophobic or hydrophilic molecules was demonstrated. Potential uses in photothermal therapy were studied using a hydrophobic indolizine cyanine dye (C3).[29] Finally, the cytotoxicity of C3-loaded nanoparticles was evaluated with human embryonic kidney (HEK) and Drosophila (S2) cells by lactate dehydrogenase (LDH) assay.

EXPERIMENTAL SECTION

Materials and Methods. Common solvents and reagents were purchased from commercial suppliers and used as received without additional purification. Tetrahydrofuran (THF) and *N*,*N*-dimethylformamide (DMF) were purified using a solvent purification system. PAMAM-G3-Boc and C3 were prepared as previously reported.[15,29] All of the synthetic procedures were conducted under an ultrapurified nitrogen atmosphere using standard organic synthesis techniques (e.g., Schlenk line) unless otherwise specified. Chloroform (99.9%, Acros), chlorobenzene (99.8%, Sigma-Aldrich), and ε-caprolactone (99%, BTC) were distilled over CaH_2. Tin(II) 2-ethylhexanoate ($Sn(Oct)_2$, 92.5−100%, Sigma-Aldrich) was dried under high vacuum (−100 kPa) for 5 days before use. The macroinitiator (PAMAM-G3-Boc) used for ring-opening polymerization (ROP) was freeze-dried prior to use. All starting materials used for the ROP were weighed in a glovebox. $^1H(^{13}C)$ NMR spectra were collected on a 300 or a 400 MHz spectrometer [Bruker Avance spectrometers (Bruker, Germany)]. Chemical shifts (δ) are denoted in parts per million (ppm) relative to an internal standard (tetramethylsilane—TMS) and referenced to a protonated solvent obtained from Cambridge Isotope Laboratories, Inc. ($CDCl_3$: δH 7.26 ppm, δC 77.16 ppm; MeOD: δH 3.31, 4.87 ppm, DMSO-d_6: δH 2.50 ppm, δC 39.52 ppm). Abbreviations used are s (singlet), d (doublet), t (triplet), q (quartet), m (multiplet), and/or b (broad). A JEOL 1230 TEM was used at 100 kV to obtain electron microscopy images using a bottom-mounted charge-coupled device (CCD) camera (Gatan Orius 831). Samples were prepared 1 day in advance and then filtered and diluted within 1 h of the experiment. For the room-temperature TEM, carbon-coated, 300 mesh grids were plasma-cleaned just before applying the sample solution. Negative staining was carried out immediately, followed by applying a 1% uranyl formate solution to the grid. For the cryo-TEM, grid freezing was achieved by using a Mark IV Vitrobot (FEI Co., Hillsboro, OH). Blotting parameters were optimized for each sample: usually, two, 1-s blots with a force of 0, +1, or +2 or alternately one, 2-s blot with a force of 0 or −3. Prepped grids were kept in liquid nitrogen until moved to a 626 Single Tilt (Gatan Inc., Pleasanton, CA) cryo transfer holder. Grids were imaged via a JEOL 1230 TEM, using a 100 kV accelerating voltage. Images were captured with a CCD camera (Gatan 831 Orius) and analyzed using the Digital Micrograph software. Tissue culture cells were grown under standard conditions. HEK293 cells were cultured in standard Dulbecco's modified Eagle's medium (DMEM) media containing 10% fetal bovine serum (FBS) and antibiotics (e.g.,

https://dx.doi.org/10.1021/acsabm.0c00432
ACS Appl. Bio Mater. 2020, 3, 5664−5677

Scheme 1. General Synthetic Route to LDBCs, PCL-G3; Example of 90:10 (90-PCL-G3) LDBC Obtained by ROP of ε-Caprolactone Monomer Initiated by a PAMAM-G3-Boc Macroinitiator (1) to Yield PCL-G3-Boc (2), Which Is Then Deprotected to Afford the Final Amphiphilic PCL-G3 LDBC (3)

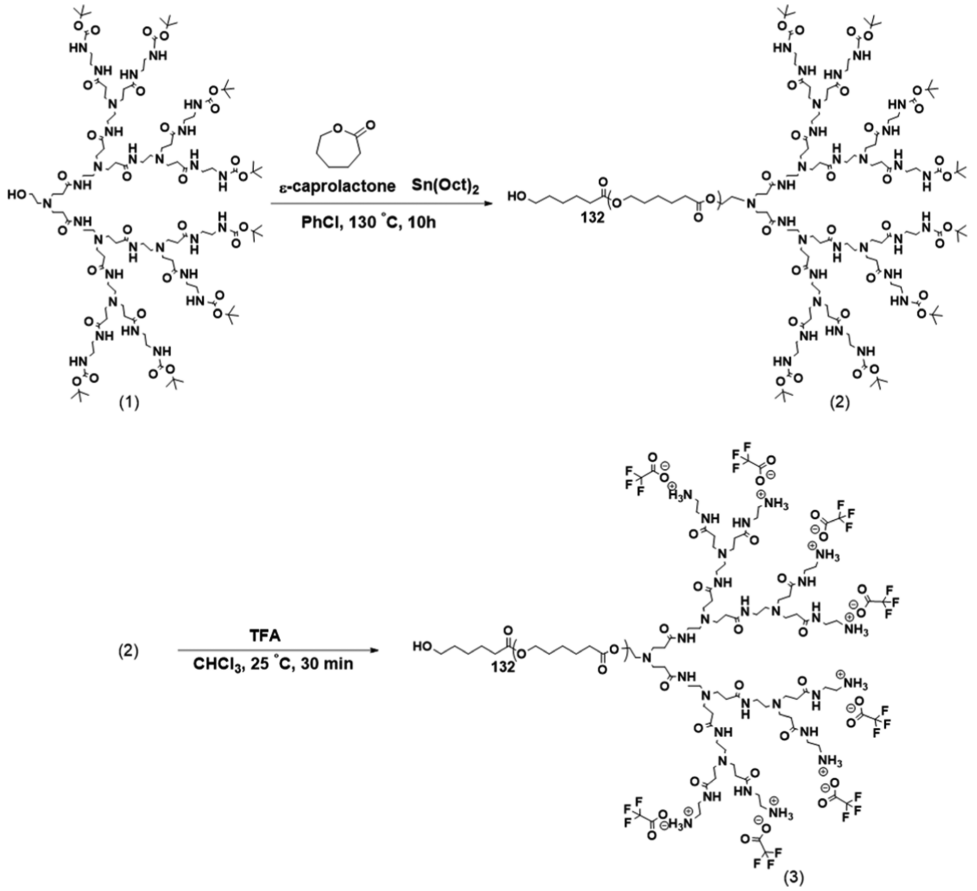

penicillin/streptomycin) under a 37 °C CO_2-injected incubator. Drosophila S2 cells were kept in Schneider media containing antibiotics (e.g., penicillin/streptomycin) and 10% FBS. S2 cells were grown at 26 °C.

General Synthesis. As outlined in Scheme 1, a generation 3 PAMAM dendron with a hydroxyl focal point (PAMAM-G3-Boc) was utilized as the macroinitiator for the ROP of ε-caprolactone to synthesize the linear segment of the block copolymer. The PAMAM dendron was synthesized according to a previously reported procedure in which ethanolamine acted as the focal point.[15] To preserve the hydroxyl focal point as the principal nucleophile, the terminal amine groups were protected with di-*tert*-butyl dicarbonate (Boc).[15] Boc-protected LDBC intermediates (i.e., before making the dendritic portion hydrophilic) were made by the ROP of ε-caprolactone, employing $Sn(Oct)_2$ as the catalyst. Different weight ratios of the LDBC intermediates with respect to PCL (i.e., 90, 70, and 50%) were obtained by varying the feed ratio for the lactone monomer. In regard to the total weight of the amphiphilic (Boc-deprotected) block copolymer, note that the percentages denote the weight ratio with respect to the hydrophobic segment. As an example, when an LDBC is labeled as 90%, the nomenclature indicates that the hydrophobic polymer segment (PCL) contains 90% of the weight of the block copolymer: 90-PCL-G3. Amine Boc protection was removed using trifluoroacetic acid (TFA) to make the dendritic portion hydrophilic and obtain amphiphilic LDBC systems (abbreviated as PCL-G3 in the main text).

Characterization of Boc-Protected Intermediates. Proton NMR spectra of all intermediates (PAMAM dendrons and Boc-protected) were collected using a Bruker Avance spectrometer (Bruker, Germany) operating at 400 or 300 MHz. Either MeOD, DMSO-d_6, or $CDCl_3$ was used as the solvent with TMS as an internal standard. The degree of polymerization (DP) of PCL was calculated by ^{1}H NMR. The molecular weight and the polydispersity index (PDI) of each LDBC intermediate were obtained via gel permeation chromatography (GPC) using DMF as the mobile phase. GPC measurements were carried out on a Waters Alliance HPLC System at 50 °C at a flow rate of 0.3 mL/min using a 2695 Separation Module equipped with 2 Tosoh Bioscience columns (TSKgel Super HM-M), a Waters 2414 DRI, and a Waters 2998 Photodiode Array Detector (PDA). The data was evaluated using Waters Empower 3 software. The GPC system was calibrated using polystyrene standards.

Preparation and Characterization of Self-Assembled Aggregates. Thermogravimetric analysis (TGA) and differential scanning calorimetry (DSC) analysis were employed to evaluated the thermal stability of the LDBCs. For each sample, a platinum pan was used, and the thermal studies were conducted under a nitrogen atmosphere at temperatures ranging from 25 to 400 °C at a ramp rate of 15 °C/min. The results were analyzed using the MUSE Analysis software. A TA Instruments DSCQ1000-0620 v9.9 was used to collect DSC scans at ramp rates of 20 °C/min with three heating/cooling cycles. The data was analyzed using TA Instruments software, Universal Analysis 2000 4.4A.

The LDBCs possessing weight ratios of 90:10, 70:30, and 50:50 (with reference to PCL) were formed into nanoparticles by employing nanoprecipitation.[30,31] Using a glass vial, THF (200 μL) was added as the organic solvent to dissolve 1 mg of LDBC. The resulting solution was added (dropwise) to a second vial containing MilliQ water (1 mL) while gently stirring and sonicating. THF was removed by allowing it to evaporate under constant airflow. Formulations were allowed to equilibrate for 12 h before testing.

Nanoparticle size and zeta potential (ζ-potential) measurements were conducted on a Zetasizer Nano ZS (Malvern Instrument) using

https://dx.doi.org/10.1021/acsabm.0c00432
ACS Appl. Bio Mater. 2020, 3, 5664−5677

a He−Ne laser (633 nm) detector angle of 173° at 25 °C. The nanoparticle concentration was 1 mg/mL, and all measurements were done in triplicate to ensure consistency. The morphological study of the aggregates formed from the LDBCs was carried out by environmental TEM and cryo-TEM.

CAC measurements were acquired via fluorescence spectroscopy and DLS. The fluorescence probe method was carried out according to a previously reported procedure.[15] A series of eight concentrations ranging from 10^{-8} to 10^{-1} mg/L were used for the experiment. The fluorescence spectra were collected on a Varian Cary fluorescence spectrometer (Agilent Technologies). For the DLS method, the same concentration series was prepared, and the measurements were taken at 25 °C. The measurements were repeated three times to assure reproducibility. By plotting the intensity of scattered light as a function of polymer concentration (mg/L), the CAC was determined.

Encapsulation Studies. Rhodamine-B (RhB), curcumin, and indolizine cyanine (C3) dye[29] were separately loaded into nanoparticles. Chemical structures and absorbance profiles for each dye are included in the Supporting Information (SI). The encapsulation efficiency (EE%) and dye loading efficiency (DL%) were determined for each molecular species. For curcumin-loaded vesicles/micelles, curcumin (1 mg) and block copolymer (2 mg) were dissolved in THF (200 μL) and added dropwise to MilliQ water (2 mL) while stirring and sonicating. THF was removed by allowing it to evaporate under a stream of nitrogen. Formulations were allowed to equilibrate for 12 h, and the unloaded dye was filtered out using a 0.45 μm syringe filter. Then, water was removed by freeze-drying, and the dye-loaded nanoparticles were redissolved in THF (5 mL). The curcumin concentration was estimated by using a Cary 6000 UV−visible spectrophotometer at 423 nm based on the standard calibration curve obtained from free curcumin in THF. A similar procedure was followed for C3 dye (1 mg), and UV−visible measurements were taken at 705 nm. DL% and EE% were calculated using the following formula

$$\text{DL}\ (\%) = 100 \times \frac{(M_C)}{(M_P + M_C)}$$

$$\text{EE}\ (\%) = 100 \times \frac{(M_C)}{(M_{Ci})}$$

with M_C = mass of curcumin or C3 in the nanoparticle, M_P = mass of LDBC, and M_{Ci} = mass of curcumin or C3 initially added during nanoprecipitation.[32]

For RhB encapsulation, RhB (10 mg) was dissolved in MilliQ water (2 mL) in a vial, and the polymer (2 mg) was dissolved in THF (200 μL) in a separate vial. The polymer solution was added into the RhB solution dropwise while sonicating and stirring. The resulting mixture was dialyzed with a 3.5 kD dialysis bag in water until all of the untrapped dye escaped as determined by testing the outer solution using a UV−vis spectroscopy at 554 nm until no dye was detected. The amount of unloaded dye was calculated via a UV−vis data analysis with a standard calibration curve. Then, the encapsulated dye amount was calculated by subtracting the unloaded dye amount from the initial weight. DL% and EE% were calculated using the same formula used for the curcumin studies.

Optical Activity of C3-Encapsulated Nanoparticles. Excited-state lifetimes were obtained from femtosecond transient absorption spectroscopy (fsTAS) measurements for both C3 and C3-encapsulated. The fsTAS measurements were performed using a femtosecond transient absorption spectrometer (Ultrafast Systems Helios Fire) and a Ti:sapphire regenerative amplified laser system (Coherent Astrella). Both samples were placed in a 2 mm cuvette and excited by a 695 nm beam generated by pumping an OPerA Solo optical parametric amplifier (Coherent) with the 800 nm fundamental output of the fs amplifier. Kinetic traces were obtained by plotting the ΔA at 480 nm for both samples over time, where the transient of both the encapsulated and nonencapsulated samples strongly absorbed. Absolute quantum yields for both samples were obtained with a Horiba Quantamaster 8075-21 spectrofluorometer and an integrating sphere. A xenon lamp monochromated to 695 nm served as the excitation source.

Storage Stability of C3-Encapsulated Nanoparticles. The storage stability of C3-encapsulated nanoparticles was evaluated by means of both dynamic light scattering (DLS) and absorbance spectroscopy. For the DLS method, C3 (1 mg) and LDBC (2 mg) dissolved in THF (200 μL) were added dropwise to MilliQ water (2 mL) while stirring and sonicating. THF was removed by allowing it to evaporate under a stream of nitrogen. Formulations were permitted to equilibrate for 12 h, and the unloaded dye was filtered (removed) using a 0.45 μm syringe filter. Particle size and the PDI were measured in 24 h intervals over 5 days and then 48 h intervals up to 10 days. Measurements were carried out on a Zetasizer Nano ZS (Malvern Instrument) using a He−Ne laser (633 nm) having a detector angle of 173° at 25 °C. To evaluate the stability of the formulations, the percent change in the size and PDI was plotted against the number of days.

For the UV−vis method, the samples were prepared using the same procedure mentioned in the DLS method. Absorption intensities were obtained using a Cary 600 UV−visible spectrophotometer in 24 h intervals for 5 days and then 48 h intervals up to 10 days. To assess the stability of the formulations, the percent decrease in the maximum intensity (λ_{max}) was plotted against the number of days.

***In Vitro* Cell Uptake and Cytotoxicity Assay.** Following self-assembly, C3-encapsulated nanoparticles were added to tissue culture media. HEK293 cells were grown under standard conditions (37 °C, 5% CO_2) in DMEM media with 10% FBS. S2 cell cultures were preserved in S2 media with 10% FBS at 25 °C. Distribution of dyes following the uptake was visualized with a laser scanning confocal microscope (Zeiss LSM 510 META) following a 24 h incubation with the nanoparticles. Cells were co-stained with a LysoTracker Green DND-26 (Invitrogen) to simultaneously image lysosomes. Cytotoxicity of the nanoparticles was then determined with a CyQUANT LDH Cytotoxicity Assay Kit (Invitrogen) using a microplate reader (BioTek Synergy H1). Differences in viability between loaded and unloaded particles at different concentrations were determined by a Tukey honestly significant difference (HSD) test.

***In Vitro* Photothermal Assay.** HEK cells near 100% confluency were treated with 500 ng of polymers and incubated overnight in 5% CO_2 at 37 °C. A 633 nm laser (5 mW) was used to irradiate cells for 8 min, followed by incubation for 2 h. Afterward, cell death was assessed with a LIVE/DEAD Cell Imaging KitTM Invitrogen following the manufacturer's protocols. Confocal microscopy was then used to assess cell death through fluorescence (568 nm excitation, >580 nm emission) of propidium iodide accumulation in cell nuclei (red channel). The number of dead cells was counted in three biological replicates. A one-tailed *t*-test was used to assess the statistical significance between loaded and unloaded nanoparticles.

RESULTS AND DISCUSSION

Design and Synthesis of PCL−PAMAM LDBCs. In this work, we aim to explore the potential applications of LDBC systems based on PAMAM and polyesters. Molecular architecture design and selection of the polymer types for each block were made with a focus on potential end uses as a biomaterial. Often referred to as the "artificial protein" because of its biomimetic characteristics,[33] a G3 PAMAM dendron was used as the hydrophilic segment due to its highly branched architecture that offers unique interfacial and functional performance. Furthermore, the dendrimer interiors can be designed and modified to facilitate the encapsulation of a vast array of guest molecules via noncovalent interactions (i.e., hydrogen-bonding, ligand, or acid−base interactions).[34] For the hydrophobic segment, PCL was used. PCL-containing (as a primary component) materials have been accepted by the Food and Drug Administration (FDA) for use in surgeries, which provides evidence of safe practice in humans. PCL

https://dx.doi.org/10.1021/acsabm.0c00432
ACS Appl. Bio Mater. 2020, 3, 5664−5677

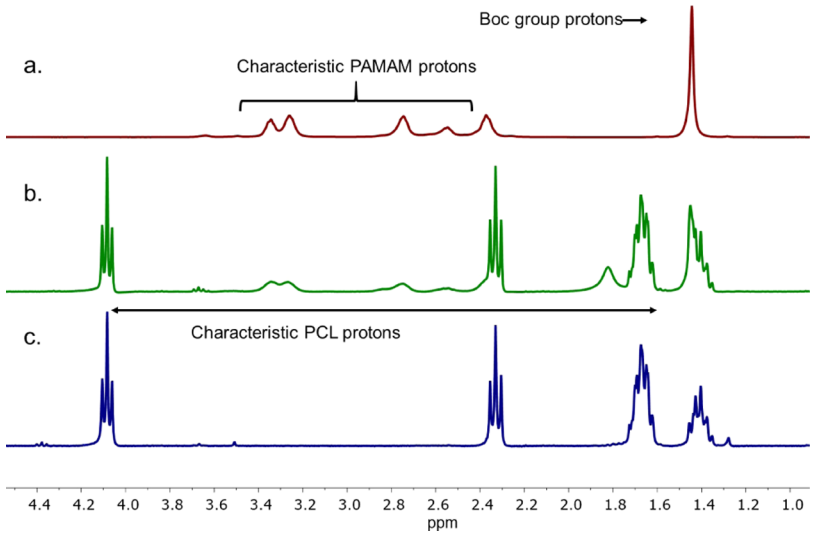

Figure 2. ^{1}H NMR overlay of the (a) macroinitiator (PAMAM-G3-Boc), (b) LDBC intermediate (70-PCL-G3Boc), and (c) LDBC after Boc deprotection (70-PCL-G3) in $CDCl_3$.

Table 1. Molecular Weight Characterization of PCL−PAMAM LDBCs of Varying Weight Ratios by GPC (Chromatograms are Shown in Figure S8)

			^{1}H NMR		GPC		
system[a]	M_{th}	DP_{th}	M_w (g/mol)	DP	M_n (g/mol)	M_w (g/mol)	$Đ$
90-PCL-G3Boc	17 465	132	18 211	138	10 185	15 902	1.56
70-PCL-G3Boc	6564	34	6564	34	5548	8850	1.59
50-PCL-G3Boc	4127	15	3944	13	3702	5733	1.56

[a]The notation of PCL-G3 denotes the LDBC composition, where PCL connected to a G3 PAMAM with a weight percentage is in respect to the lactone monomer used; M_{th}, theoretical molar mass; M_n, number average molar mass; M_w, weight-average molar mass; and $Đ$, dispersity.

exhibits a high permeability to drugs and has a lower acidic degradation rate than other aliphatic polyesters.[35] The low T_g (−60 °C) of PCL and its exceptional rheological properties make it an appropriate candidate for various applications in the biomedical field.[36]

The general synthesis of PCL-G3 is depicted in Scheme 1. Previous work has been reported on the synthesis of LDBCs via copper (Cu) click chemistry approaches. However, these approaches have limitations due to involving multistep syntheses to achieve different weight ratios of the blocks. Such protocols require excess addition of one reactant to achieve high yields and demand additional purification steps to remove the excess reactants from the reaction mixture.[37,38] Here, we took an approach that uses Boc-protected PAMAM (G3) containing a hydroxyl focal point to initiate the ROP of ε-caprolactone with a $Sn(Oct)_2$ catalyst. By changing the monomer feed ratio, a library of PCL-G3-Boc LDBCs were synthesized with mass ratios of 90:10, 70:30, and 50:50 PCL to PAMAM.

The heavy metal-containing catalyst concentration should be kept at the minimum possible level to avoid potential toxicity-related issues in biological systems. Therefore, polymerization kinetic studies were carried out to identify the minimum catalyst concentration (Figures S5−S7). We observed that the LDBC systems, which have PAMAM > 30 wt % (i.e., 70-PCL-G3 and 50-PCL-G3), required higher catalyst loading than the 90-PCL-G3 system. This may be due to the deactivation of the catalyst via coordination between the metal center and the PAMAM dendron. Additional polymerization kinetic studies are provided in the SI (Figure S7). Catalyst equivalents of 0.3−0.6 (i.e., 0.3 for 90-PCL-G3 and 0.6 for 70-PCL-G3 and 50-PCL-G3) per hydroxyl focal point were used with the LDBC systems studied here.

As shown in Figure 2, an overlay of ^{1}H NMR spectra displays characteristic resonance peaks corresponding to the Boc-protected macroinitiator (2.19−3.69 ppm; Figure 2a) and PCL (1.38, 1.64, 2.30, 4.05 ppm; Figure 2b,c) in $CDCl_3$ (Figures S1−S4). Peaks representing both blocks are shown in the spectrum of the LDBC intermediate before the Boc deprotection (Figure 2b). After the Boc deprotection, a drastic reduction in the intensity of the resonance peaks corresponding to PAMAM is observed, yet signals corresponding to PCL remained visible. The suppression of PAMAM signals is presumably due to a change in relaxation time that is caused by a phase change. Note that deprotected PAMAM exhibits a decrease in solubility when placed in an organic solvent. This insolubility leads to a solvent-driven nanoaggregation that helps to shield the hydrophilic PAMAM from the organic solvent resulting in a reverse-phase nanoaggregation, where PCL is the outer shell and PAMAM is the inner core. Upon the formation of these reverse nanoparticles, PAMAM experiences a phase change from the solution phase to the aggregation phase. This phase change can be considered as the reason for the change in the relaxation time for the PAMAM protons as it is frozen or locked in the core of the nanoparticle. Similar behavior was observed with previously reported amphiphilic LDBCs.[15,39]

Molecular Weight Analysis of LDBCs. The molar mass and DP of the Boc-protected intermediates were calculated using ^{1}H NMR spectroscopy. The characteristic PAMAM

https://dx.doi.org/10.1021/acsabm.0c00432
ACS Appl. Bio Mater. 2020, 3, 5664−5677

resonance signal at 3.30 ppm (with 46 protons) was used as the reference peak, and the PCL peak (methylene protons) at 4.05 ppm was integrated with respect to PAMAM to calculate the DP. Molar mass calculations from ^{1}H NMR were supported by the GPC data, which are given in Table 1. Since evidence of reverse aggregate formation from the LDBCs in less polar organic solvents is observed, the Boc-protected intermediates were analyzed due to the ^{1}H NMR signals appearing in a more molecular form. GPC chromatograms are included in the SI (Figure S8).

Thermal Analysis. Thermal analysis was achieved via TGA and DSC using deprotected LDBCs. In this regard, all LDBCs of study possess NH_3^+ end groups, unless otherwise noted. TGA is a well-known method for assessing polymer backbone and architectural structure.[40] The polymeric composition can be deduced by the qualitative characterization of the degradation process shown by the weight loss percentage (ΔW) and the inflection point temperature (T_d).[41] All of the measurements were taken under nitrogen conditions at a heating rate of 10 °C/min and are shown in SI (Figures S9 and S10). Two significant transitions in the slopes of the degradation curves were observed for all of the LDBCs. Each slope change corresponds to the decompositions of the phase-separated PAMAM and PCL blocks. The T_d and ΔW data (Table 2) suggest that the first degradation step is due to the PAMAM block and the second to the PCL block. For example, in 70-PCL-G3 (70 wt % PCL) (Figure 3), two weight loss steps, the former of 28% and the latter of 65%, were observed, which correlate to a theoretical weight ratio of 30:70 (PAMAM/PCL). Similar results were obtained with the other two systems (Table 2 and Figures S9 and S10). These correlations between the weight ratio of the blocks, T_d, and the weight loss percentage after each degradation step provide qualitative evidence for the reliability of the synthetic methodology employed.

Table 2. Thermal Analysis Data (TGA) Confirming the Weight Ratios for Each LDBC[a]

	composition		first step		second step	
system	PAMAM	PCL	T_d (°C)	ΔW (wt %)	T_d (°C)	ΔW (wt %)
90-PCL-G3	10	90	214	9	379	88
70-PCL-G3	30	70	216	28	312	65
50-PCL-G3	50	50	215	45	288	40

[a] T_d, inflection point temperature; and ΔW, weight loss percentage.

With the synthetic strategy established, the weight of the hydrophilic PAMAM portion was kept constant, and the weight of the hydrophobic PCL portion was changed accordingly to obtain the desired wt % ratios. The same trend can be seen when comparing the T_d values at two thermal steps. The first step corresponds to the decomposition of PAMAM and shows a minimal change in T_d values between different systems (only 1 °C fluctuation). The second step corresponds to the decomposition of PCL and shows a significant decrease of T_d between the LDBCs when decreasing the PCL weight ratio (Table 2). 90-PCL-G3, which has the highest weight ratio of PCL, shows the largest T_d (379 °C) when compared to 70 and 50-PCL-G3 with T_d values of 312 and 288 °C, respectively. This trend suggests that the molecular architecture of the LDBCs has the same PAMAM block but different PCL chain lengths. DSC thermograms

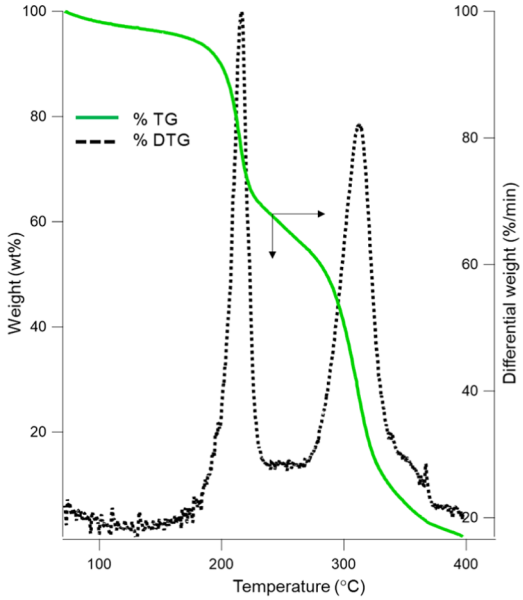

Figure 3. TGA (green) and derivative thermogravimetry (DTG) (black) thermograms for 70-PCL-G3 under nitrogen. (The arrow indicates the midpoint between the two major thermal events.).

showed a peak at 54 °C for 90-PCL-G3, which is hypothesized to be the melting temperature (T_m) of PCL in the LDBC as the reported melting point range for pure linear PCL is 59−64 °C, and the T_g of PCL homopolymer is −60 °C (Figure S11).[36] T_m was shown to decrease as a function of the polyester type and hydrophobic mass ratio. 70-PCL-G3 and 50-PCL-G3 exhibited 50.4 and 47.3 °C T_m values, respectively (Figures S12 and S13). In addition, the peak shape changes from sharp and intense to broad when the hydrophobic wt % decreases, suggesting a critical influence of the PAMAM block on the properties of the linear polyester. Such changes in polymer properties due to diblock formation are well known in the literature and point to the combinatory contribution of both PCL and PAMAM in the LDBC.[40,42,43]

Self-Assembly and Morphology. The self-assembly into nanoparticles of the LDBCs in water was done using the nanoprecipitation method.[44] The sizes and morphologies were studied using DLS (Table S1) and TEM (Figures 4 and S14 and S15). The intensity-average DLS size distribution shows that the 90-PCL-G3 LDBC forms aggregates of approximately 96.4 nm in hydrodynamic diameter (D_h), while the Z-average size shows a diameter of 77.8 nm, which indicates the presence of a smaller particle distribution as well. Cryo-TEM images (Figure 4) confirm the presence of two significant distributions of spherical particles with an average diameter of 71.1 nm, which correlates with the Z-average diameter observed from DLS. Although it is not evident from the cryo-TEM images herein, previous studies have shown that the LDBCs having hydrophobic (polyester) wt % >70% form bilayer vesicles.[15,45,46] Uranyl formate was used as a contrasting agent to improve the visibility of the PCL bilayer. The contrasting agent accumulates more in the dense polyester bilayer, and this can be seen as a darker region in the room-temperature TEM image (Figure S14). Using these lighter and darker regions of the TEM image, indirect evidence can be obtained about layered vesicle morphologies.[47]

Aggregates formed from 70-PCL-G3 LDBCs exhibited high polydispersity with an average D_h of 45.6 nm and a PDI of

https://dx.doi.org/10.1021/acsabm.0c00432
ACS Appl. Bio Mater. 2020, 3, 5664−5677

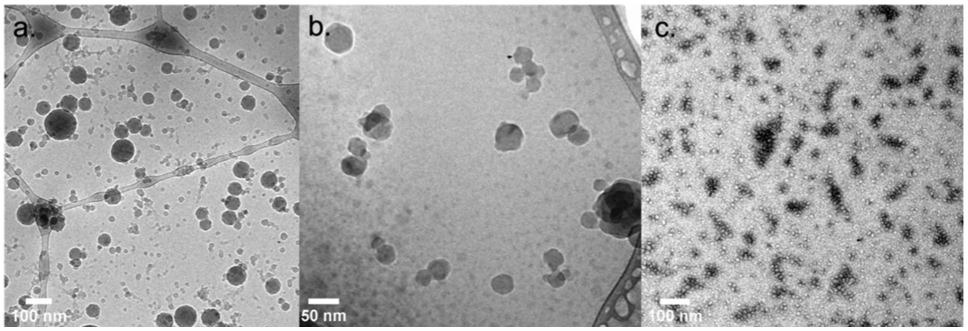

Figure 4. Nanoparticles formed by (a) 90-PCL-G3, (b) 70-PCL-G3, and (c) 50-PCL-G3 under cryo-TEM, 1% uranyl formate as the contrast agent. Additional analysis is included in the SI (Figures S14 and S15).

0.50. Size distribution by intensity shows a polymodal distribution with two significant sizes of 51.6 and 359.4 nm, which result from the secondary aggregation of regular nanoparticles. This hypothesis was supported by TEM images, which show two major size distributions of spherical shaped particles with average diameters of 48.1 and 29.8 nm. Additional secondary clusters made of smaller particles correspond well with the polymodal distribution observed in DLS (Figure S15). Furthermore, additional TEM images with a contrast agent suggest vesicle morphologies for these spherical shaped particles formed by 90-PCL-G3 and 70-PCL-G3 LDBC systems (Figure S14).

In comparison with 90 and 70, 50-PCL-G3 also showed a high polydispersity of 0.53 and a polymodal distribution in the DLS intensity plot, where the major distribution showed a D_h of 221.4 nm and a minor distribution of 16.7 nm. The majority of the particles were seen as clusters in the TEM images, which explains the high polydispersity and larger size DLS distributions. Isolated particles from the clusters showed a spherical shape with an average diameter of 14.0 nm and assumed to be core−shell micelles because the PCL bilayer was not visible in the TEM images (Figure S15b). The morphological evidence obtained from the TEM analysis was further supported by encapsulation studies described below.

When considering the sizes of the individual particles (isolated particles form clusters), a decreasing trend was observed, and more aggregation of the particles into clusters was shown. We hypothesize that the smaller particles (70-PCL-G3 and 50-PCL-G3) tend to form larger aggregates to decrease the relative surface energy, while the LDBC solution that has larger particles (90-PCL-G3) shows minimum secondary aggregation. It is well established that there is an inverse proportional relationship between the diameter of the spherical nanoparticles and the relative surface energy.[48,49] This postulation can be further supported by the Brownian agglomeration mechanism. In this case, the formation of larger aggregates results from particles colliding and fusing as a result of their random motion.[50] For this study, temperature (the main factor affecting Brownian motion), sample volume, and material concentration were kept constant among all of the trials. Therefore, the smaller particles should have higher kinetic energy than the larger particles and thus gain higher velocities. This leads to a higher collision rate of the particles and makes more aggregates/clusters in the systems that have smaller nanoparticles.[50]

The observed morphologies follow previously reported and established morphological trends, which can be explained using the packing of the copolymer chains and molecular curvature.[45,46,51−53] The packing parameter (p), established by Israelachvili et al. and defined in eq 1, combines copolymer properties to predict the curvature and the prepared morphologies[52−55]

$$p = \frac{v}{a_o L_c} \tag{1}$$

In eq 1, v is the volume of the hydrophobic chains, a_o is the optimal area of the head group (hydrophilic PAMAM block in our case), and L_c is the hydrophobic chain length. According to the theories of self-assembly, p should be less than 1/3 to form spherical micelles and between 1/2 and 1 to form vesicles/polymersomes.[46,51,52,55] For these LDBCs, a_o remains constant because the hydrophilic block is the same for all systems. Therefore, p is defined by the weight ratio of the hydrophobic block. When the weight ratio of the hydrophobic block is ≥70%, the higher volume and length lead to the formation of vesicle-like structures. Spherical micelle structures obtained from 50-PCL-G3 can also be explained similarly.

Surface charges (ζ-potential) of the nanoparticles ranged from 37.0 to 72.4 mV. The lowest ζ-potential value was obtained for the 90-PCL-G3 system, which showed the highest monodispersity and did not have larger secondary aggregates. For the other two LDBC systems that had larger secondary aggregates, higher surface charges were observed (Table S1). This trend can be explained from the ζ-potential distribution plots of each system, where 90-PCL-G3 shows a monomodal and a narrow distribution that correlates with the PDI observed from DLS. Nevertheless, for 70-PCL-G3 and 50-PCL-G3, bimodal/polymodal distributions are observed with peaks corresponding to higher surface charges, which are assumed to be from the larger secondary aggregates (Figures S19−S21). Such values are viewed as highly stable in colloidal research, and those of 20−30 mV are prevalent in the drug delivery literature.[56,57] In general, positively charged nanoparticles can penetrate cell membranes easily since they are commonly known to be negative.[58,59] Since the high ζ-potentials for the LDBC nanoparticles are concerning, *in vitro* cytotoxicity studies were undertaken. These studies (*vide infra*) show that the cell death induced by these polymeric nanoparticles is ≤15% at the highest concentrations, which provides a preliminary indication that these materials are nontoxic to biological systems.

The CAC for the LDBCs ranges from 0.67 to 6.16 mg/L as determined by a fluorescent probe (pyrene), which provides further evidence of stable nanoparticles. DLS analysis shows a nonlinear relationship between LDBC concentration and scattering intensity, confirming the presence of nanoscale

https://dx.doi.org/10.1021/acsabm.0c00432
ACS Appl. Bio Mater. 2020, 3, 5664−5677

vesicles/micelles above the CAC (Figure S22). The CAC varied among the LDBC systems, with an observed dependence on hydrophobic wt %. The CAC is one of the basic parameters that defines the thermodynamic stability of a nanoparticle. Lower CAC values indicate higher thermodynamic stability. When the polymer chains have a higher number of points of interactions, higher thermodynamic stability is gained and leads to lower CAC values.[13] Lower CAC values were exhibited by LDBCs, which have longer PCL chains. The CAC for 90-PCL-G3 (0.67 mg/L) was the lowest (10-fold lower than 50-PCL-G3, 6.2 mg/L) due to its increased hydrophobic interactions among the longer PCL chains.[32,60] The values for 70-PCL-G3 and 90-PCL-G3 (Figure S22) are analogous to those found in the literature and correlate to their potential as exceptional biomaterials.[61−63]

Encapsulation Studies. As our goal is to evaluate the potential of these nanoparticles as carriers in therapeutic delivery and/or theranostics, the ability to uptake hydrophobic or hydrophilic molecules was studied. As a hydrophobic drug model, curcumin, chemically referred to as diferuloylmethane (Figure S23), was selected. This is a highly hydrophobic small molecule that exhibits antioxidant, anti-inflammatory, and anticancer properties.[64,65] Because aggregates formed from 90-PCL-G3 and 70-PCL-G3 show evidence of bilayer vesicle formation in an aqueous medium, we hypothesized that these LDBCs would improve the water solubility of curcumin via the encapsulation into the PCL bilayer of the vesicle. Figure 5 validates the solubilizing abilities of the LDBCs (Figure 5a) and enhanced drug-applicable curcumin loaded in all three LDBC systems (Figure 5b−d).

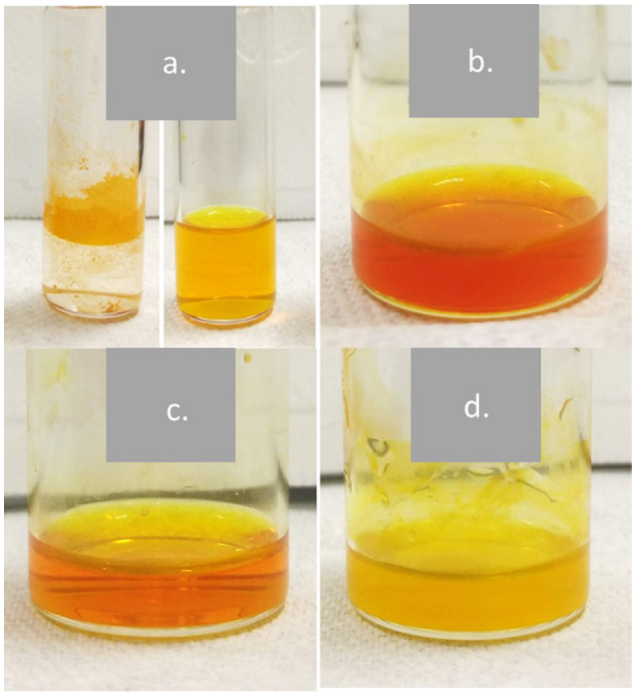

Figure 5. (a) Left, a dispersion of curcumin in H_2O; and right, curcumin-loaded 90-PCL-G3, (b) magnified image of curcumin-loaded 90-PCL-G3, (c) curcumin-loaded 70-PCL-G3, and (d) curcumin-loaded 50-PCL-G3. (Curcumin and the LDBC concentrations were kept at 0.5 and 1.0 mg/mL, respectively, for all of the systems.).

In the absence of 90-PCL-G3, curcumin is entirely insoluble. Figure 5a (left) shows where precipitated curcumin is visible at the bottom of the tube and adheres to the sample vial as a separate layer on the water surface. In contrast, the encapsulation of curcumin in 90-PCL-G3 nanoparticles (Figure 5a, right) provides a homogeneous and transparent yellow-orange solution. As shown in Figure 5b,c, LDBCs containing hydrophobic portions at ≥70 wt % increased the solubility of curcumin by giving clear homogeneous solutions, while 50-PCL-G3 system exhibits a highly turbid solution with sedimentation on the bottom of the vial (Figure 5d). The presence of longer hydrophobic chains results in a significantly higher EE% and DL% of curcumin (Table S2). This observation correlates with the morphological differences observed in TEM analysis. Nanoparticles showing the evidence of bilayer vesicle morphologies (70-PCL-G3 and 90-PCL-G3) encapsulated more curcumin and increased its solubility. Furthermore, 90-PCL-G3 showed an enhanced DL% and EE% toward curcumin than 70-PCL-G3, which suggests that the higher hydrophobic wt % LDBCs more efficiently load hydrophobic molecules. Encapsulation of curcumin in the hydrophobic bilayer of the 90-PCL-G3 particles leads to an increase in D_h from 96.4 to 255.5 nm as determined with DLS, suggesting an expansion of the particles upon encapsulation of curcumin. Another possibility for this size expansion is secondary aggregate formation upon the encapsulation. However, the monomodal size distribution and 0.10 PDI in DLS suggest that 90-PCL-G3 particles, upon loading, formed no secondary aggregates (Figures S16 and S17). DLS analysis of before and after encapsulation with 70-PCL-G3 shows a size increase consistent with secondary aggregation from 359.4 to 550.5 nm after the encapsulation, which is an indication of smaller aggregates forming larger secondary aggregates.[66,67] In contrast with 90-PCL-G3, isolated vesicles (first distribution in DLS; Figure S17) of 70-PCL-G3 did not show a significant increase in size (only a 4 nm increase of D_h), which was expected due to its relatively low loading efficiency (Table S2). The DL% of 50-PCL-G3 is insignificant at ≤1% due to its shorter hydrophobic chain and smaller particle size. Furthermore, there was no increase in particle size after curcumin encapsulation. It is interesting to note that the 90-PCL-G3 can uptake the hydrophobic drug (curcumin) up to 21.7 DL% without making secondary aggregates while keeping the PDI at 0.10, which is a positive indication of its potential to be utilized in therapeutic delivery applications.

Rhodamine-B (RhB) (Figure S23), an amphoteric dye and fluorochrome, was used to evaluate the uptake of hydrophilic molecules. Both 90-PCL-G3 and 70-PCL-G3 systems showed high DL% for RhB. There are three possible sites where hydrophilic molecules can be loaded into the vesicles of 90-PCL-G3 and 70-PCL-G3 LDBC systems: (1) the water pocket that is trapped in the vesicle, (2) the inner PAMAM layers, and (3) the outer PAMAM layers (Figure 1). 50-PCL-G3 has a lower DL%, which can be explained by the lack of both the water pocket and the inner PAMAM layer because of the micelle morphology and the smaller particle size. This observation provides indirect evidence for the morphologies deduced from TEM analysis. When comparing the 90-PCL-G3 and 70-PCL-G3 systems, both have the same DL% values even though the particles of 70-PCL-G3 are smaller in size before the encapsulation. Interestingly, the 70-PCL-G3 particle size has expanded and reached the same size as the 90-PCL-G3 system after dye encapsulation, which explains the similar

https://dx.doi.org/10.1021/acsabm.0c00432
ACS Appl. Bio Mater. 2020, 3, 5664−5677

encapsulation behavior of both systems. In addition, a decrease in surface charge (down to a range between 24.2 and 39.6 mV) was observed for all three systems after the encapsulation of RhB, which can be an added advantage in potential therapeutic delivery applications. This observation is yet to be explained, and experiments with different hydrophilic molecules and computational modeling are actively being carried out.

Benchmark Studies with Cyanine-Based Photothermal Imaging Agent C3. The preliminary encapsulation studies with curcumin and RhB provide substantial evidence of the ability of the LDBCs to uptake both hydrophobic and hydrophilic molecules separately. Aiming to apply the LDBC materials toward theranostics, we sought to increase the solubility of a hydrophobic photothermal/imaging agent and study the cellular uptake and toxicity of the agent-loaded LDBCs. Recently, the reported near-infrared (NIR) emissive cyanine dye C3 was selected for these studies.[29] Cyanine-based dyes are commonly used as imaging agents for photoacoustic (PAI) and near-infrared fluorescence (NIRF) imaging. They are capable of transforming absorbed NIR photons to heat as a photothermal (PT) agent and to lower energy NIR photons for an image-guided combinatorial phototherapeutic agent. However, several bottlenecks limit the application of cyanine dyes, such as solubility and instability in aqueous media, which decrease their imaging and therapeutic potential.[68−70]

As a benchmark for the application of LDBCs in photothermal therapy, hydrophobic cyanine dye C3 (Figure S23) was encapsulated in the 90-PCL-G3 and 70-PCL-G3 systems. The dye is not soluble in water, but encapsulation in LDBCs increased its solubility dramatically (Figure 6a,c) to

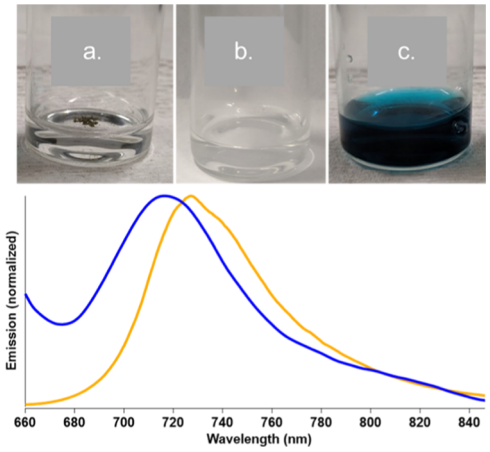

Figure 6. Top: dispersion of C3 in (a) water, (b) 70-PCL-G3 in water (by nanoprecipitation), and (c) C3 encapsulated in 70-PCL-G3 LDBC nanoparticles in water. Bottom: vis−NIR emission overlay of the dye in 1:1 ACN/H_2O (yellow) and encapsulated nanoparticles in water (blue) with excitation at 650 nm. (C3 and the LDBC concentrations were kept at 0.5 and 1.0 mg/mL, respectively, for all of the systems.).

afford DL% values of 4.3% for 90-PCL-G3 and 1.7% for 70-PCL-G3. As the dye is insoluble in water, absorption, emission, and the lifetime of the free dye were evaluated in a mixture of ACN/H_2O (1:1) and compared with the encapsulated dye in water. Nonencapsulated C3 has a low-energy absorbance maximum wavelength (λ_{max}^{abs}) and emission wavelength maxima (λ_{max}^{emis}) of 696 and 728 nm, respectively (Figures 6 and S23). C3-loaded nanoparticles show only modest shifts of λ_{max}^{abs} and λ_{max}^{emis} with values of 693 and 720 nm, respectively, in water. However, the absorption profile of the dye does change significantly with a dramatic broadening of the absorption curve from a half-peak height width of ∼80 nm to a half-peak height width of ∼200 nm upon encapsulation. Additionally, the higher-energy vibronic shoulder shifts from approximately 25% of the λ_{max}^{abs} peak height to approximately 80% of the λ_{max}^{abs} peak height upon encapsulation. This broadening and vibronic shoulder increase in intensity are indicative of cyanine-type dye aggregation, as can commonly be observed from neat films or at interfaces.[71,72] Notably, the emission curve shape did not change in a similarly dramatic way relative to the absorption curve shape upon encapsulation. The quantum yields for nonencapsulated and encapsulated C3 were measured to be less than 1%. Such values are not uncommon for cyanine dyes in water with exceptionally popular dyes such as indocyanine green, which is FDA-approved and has been used routinely in surgical/diagnostic settings for multiple decades.[73] Furthermore, the lifetime (τ) of the excited state was evaluated before and after encapsulation (Figure S24). The kinetic trace for the nonencapsulated C3 solution was fit using a single-exponential decay function and gave a lifetime of 10.24 ps. The C3 LDBC system was fit using a double exponential with a short component of τ = 11.47 ps and a longer component of τ = 106.51 ps. The double-exponential nature of the encapsulated C3 suggests either the presence of both the free dye and its encapsulated form during measurements or a dynamic process occurring upon photoexcitation. Given the dramatically longer lifetime of C3 when encapsulated, the nanoparticles are capable of inducing an extended excited-state lifetime of an encapsulated dye. This is most likely due to an increased delocalization of the excited state due to C3 molecular aggregation occurring inside of the nanoparticle.[74]

The storage lifetime of the delivery system (carrier of the therapeutic agent) is a crucial factor in biomedical applications. For the LDBC nanoparticles, the change in the PDI and the size of the nanoparticles (with no C3 loading) were insignificant after 10 days (Figure S25), and no visual variances (i.e., no color change or precipitate) were observed. This indicates that the nanoparticles, without any dye loading, are stable in an aqueous media for up to a minimum of 10 days. Upon C3 encapsulation (loading with the dye), an increase in PDI (increase by 0.037 for 70-PCL-G3 and 0.184 for 90-CL-G3) and a change in particle size (<10 nm) were observed. Similar changes in particle size and dispersity upon loading have been observed.[75−77] After the encapsulation of C3, the PDI remained without a significant change for 5 days, but a 0.03 increase in PDI was observed between the fifth and seventh days of testing. The particle sizes remained within a normal distribution between 53.2 and 63.8 nm for 7 days (Figure S25). In addition, we monitored the percentage of the encapsulated dye remaining in the nanoparticles in 12−24 h intervals using UV−vis−NIR absorbance spectroscopy. LDBC nanoparticles were able to hold approximately 80% of the encapsulated dye after 5 days. Almost a 50% drop of absorbance intensity was observed between the 5th and 10th days, which shows that the majority of the loaded dye is released after 5 days. The combined results from the DLS and absorbance spectroscopy indicate that the C3-encapsulated nanoparticles are stable up to 5 days after the preparation. Without specific preservation techniques such as PEGylation or lyophilization, the observed storage lifetimes are impressive

https://dx.doi.org/10.1021/acsabm.0c00432
ACS Appl. Bio Mater. 2020, 3, 5664−5677

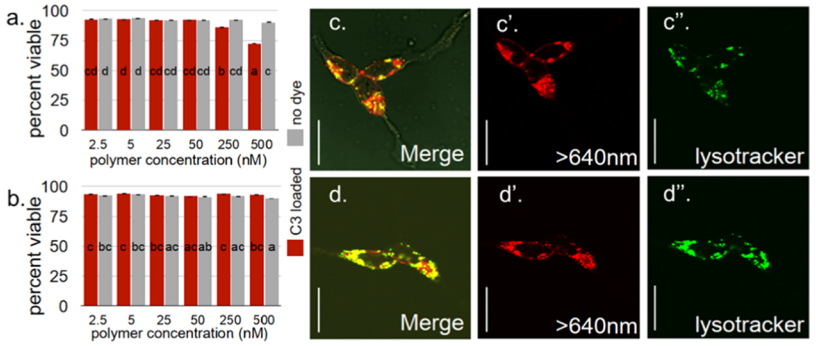

Figure 7. Cell viability after treatment with 90-PCL-G3 (a) and 70-PCL-G3 (b). Cytotoxicity (percentage) was determined by the LDH assay. Error bars denote the standard error, while letter denotes significance groups as determined by Tukey HSD ($p \leq 0.05$). HEK cells after exposure to dye-loaded nanoparticles (c, c′, 90-PCL-G3; and d, d′, 70-PCL-G3) and LysoTracker green. The left panels (c, d) are a merge of the bright field with LysoTracker (green) and C3 (red) with overlap coefficients of 0.74 and 0.85, respectively, which shows colocalization between C3 fluorescence and LysoTracker. The right panels (c′, d′) are the C3 dye fluorescence alone and (c″, d″) are the LysoTracker fluorescence panels (scale bar = 25 μm).

and quite comparable to similar liposome-like nanoparticles that have undergone cargo loading.[78−80]

***In Vitro* Cytotoxicity.** The cytotoxicity of empty and C3-loaded nanoparticles was tested in HEK and S2 cell lines. HEK cells were selected as a representation of human cell interactions, and S2 fruit fly cells were selected to represent nonhuman animal cell interactions (Figures 7 and S26). After treatment with 90-PCL-G3 and 70-PCL-G3 formulations without C3, the cell viability was above 90 and 85% at the highest concentration (500 nM) for HEK cells and S2 cells, respectively (Figures 7 and S26; Table S3), which suggest a general nontoxicity for both copolymers. Noticeably, however, there is a lower cell survival rate of S2 cells at lower concentrations of LDBCs. This can be explained by the properties of the cell. S2 cells have been described as macrophage-like cells; thus, they exhibit higher and more efficient uptake properties relative to HEK cells.[81,82] As a result, higher toxicity is observed for the S2 cells due to a more efficient uptake of free polymer.

There was no significant increase in cell death with C3-loaded nanoparticles at the same conditions, with the exception of 90-PCL-G3 loaded with C3 introduced to the cell environment in the highest concentration studied at 500 nM, where a modest reduction of cell viability of 17% is observed (Figure 7 and Table S3). This could be a consequence of some instability *in vivo* for this particular formulation or LDBC (i.e., higher hydrophobicity content than 70-PCL-G3) that results in a release of C3 or precipitation of the polymer aggregates, which perturbs cellular processes.[83] Together, these results indicate that the encapsulation of the selected imaging/photothermal agent does not induce significant cytotoxicity at varied concentrations (Figure 7a,b).

As a potential cell imaging and phototherapeutic agent, cellular internalization was evaluated by measuring fluorescence signals generated by C3-loaded nanoparticles within S2 and HEK cells via confocal microscopy (Figures 7 and S26). Additionally, LysoTracker (green) was used to visualize lysosomes and to assess the intercellular trafficking of cells after treatment with dye-loaded nanoparticles (Figure 7c,d).[84,85] When overlapping the emission of LysoTracker and the encapsulated NIR agent (Figure 7c,d,c′,d′), both fluorescence signals are observed from the same regions of the cells with overlap coefficients of 0.74 and 0.85 for 90-PCL-G3 and 70-PCL-G3 loaded with C3, respectively. Fluorescent signals associated with C3 could be observed in HEK cytoplasmic bodies, which partly overlaps with lysosomal signals. This suggests a model where polymers interact electrostatically with cellular membranes, followed by an entrance into endosomes through routine internalization of membranes. Once in the endomembrane system, the nanoparticles become trafficked, in part, to lysosomes. Similar observations are made when analogous studies were conducted with S2 cells with overlap coefficients of 0.61 and 0.74 for 90-PCL-G3 and 70-PCL-G3 loaded with C3, respectively (Figure S26). The uptaken nanoparticles seen by the assay provide supporting evidence confirming the low toxicity of the LDBC materials with the loaded imaging/photothermal agent. Such observations act as indirect evidence that dye-loaded nanoparticles are accumulated in lysosomes affording visualization of the cellular compartment. As the polymers are designed from biodegradable components, degradation of the nanocarrier is expected to occur inside the lysosomes after imaging with low toxicity. Further work is needed to study the biological degradation of these materials and planned as a follow-up study to this work.

Given the high molar absorptivity and emissive quantum yield, C3 is expected to be a good photothermal therapy dye.[29] The preliminary phototherapeutic efficacy of C3-loaded nanoparticles was evaluated *in vitro*. To assess the photothermal capacity, a series of C3-loaded nanoparticles with different concentrations were irradiated (633 nm), and the temperature change was monitored (Figure S27). The photothermal measurements were conducted as the temperature change of a bulk solvent using a temperature probe in a dilute solution of the material. Results indicate a less than 5 °C increase in temperature relative to a control sample (empty PCL-G3 nanoparticles). Figure 8 summarizes the metabolic activities of the HEK cells treated with C3-loaded nanoparticles with and without NIR exposure. HEK cells treated with C3-loaded nanoparticles of 90-PCL-G3 and 70-PCL-G3 (500 nM) and irradiated with NIR light for 8 min showed appreciable cell death. Results of the *in vitro* photothermal assay indicate that for both 90-PCL-G3- and 70-PCL-G3 C3-loaded nanoparticles, an increase in cell death is achieved after laser exposure when compared to cells treated with laser irradiation alone. Figure 8a,b shows an increased number of dead cells marked by red fluorescence after laser exposure, while Figure 8c demonstrates a statistically significant differ-

https://dx.doi.org/10.1021/acsabm.0c00432
ACS Appl. Bio Mater. 2020, 3, 5664−5677

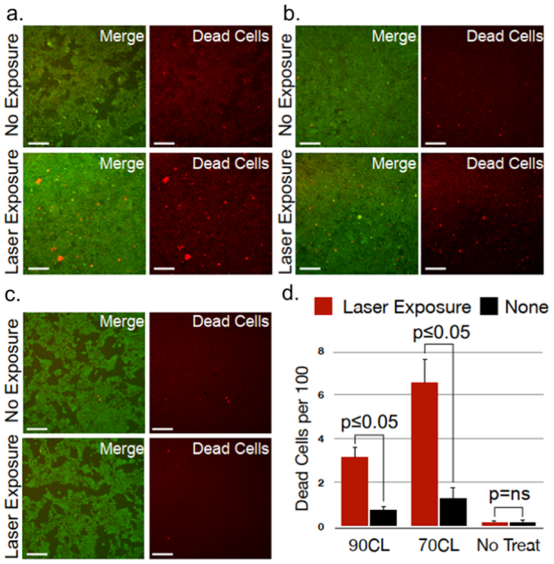

Figure 8. C3-loaded nanoparticles of (a) 90-PCL-G3 and (b) 70-PCL-G3, respectively, with HEK cells shown before (green) laser exposure and after (red) exposure. (c) Control with no nanoparticle loading (scale bar = 200 μm). (d) Cell death count before and after laser exposure with and without nanoparticles.

ence in the number of dead cells before and after irradiation. The results yield promising evidence of utilizing C3-loaded nanoparticles, where PCL−PAMAM LDBCs act as carriers for photothermal and imaging applications. While the observed photothermal activity displays promise, additional studies are needed to afford a highly efficient photothermal dye and polymer construct.[86,87]

CONCLUSIONS

Amphiphilic PCL−PAMAM LDBCs are attractive for the development of potential therapeutic delivery systems to be utilized in nanomedicine. A feasible and robust synthetic strategy was employed to construct a series of LDBCs by changing the chain length of the hydrophobic segment. In addition to the conventional structural characterization with NMR and GPC, thermal analysis provided qualitative evidence for the reliability of the synthetic strategy. According to the variations in hydrophilic-to-hydrophobic weight ratios, we observed various morphologies for their nanoparticles in water. Evidence of polymersomes (bilayer vesicles mimics of biological vesicles) was observed for LDBCs above 70% hydrophobic (PCL) wt %, and these materials have the potential to be used as biocompatible carriers in nanomedicine. The CAC studies provide further evidence for the stability of the nanoparticles.[88] The CAC values for 70-PCL-G3 and 90-PCL-G3 are similar to those reported in the literature and correlate well to the capacity of the copolymers as efficient biomaterials.[89−91] Preliminary studies showed that the LDBC nanoparticles can uptake a hydrophobic therapeutic agent up to 21.7 DL% without destabilizing the nanoparticle. Furthermore, high loading (63% DL) efficiencies toward RhB indicate that these nanoparticles can be employed to deliver either hydrophilic or hydrophilic therapeutic agents.

Aiming to apply the material toward theranostics, we were able to increase the solubility of a hydrophobic photothermal/imaging agent, C3, by loading it into LDBC as nanoparticles. These dye-loaded nanoparticles were successfully uptaken by HEK and S2 cells without inducing significant cell death. Even though the nanoparticles show positive surface charges, demonstrating minimal cell toxicity provides evidence for the biocompatibility of the nanocarriers. We were able to induce cell death by exposing the C3 dye (loaded into cells via encapsulation in nanoparticles) to an NIR laser. Photothermal studies of cell death after treatment with C3-loaded nanoparticles and upon laser exposure support a significant cell death relative to control samples that were not exposed. This is a positive and firm indication of the potential of these materials as nanocarrier in nanomedicine. Ongoing research is aimed toward the assembly of interesting LDBCs, utilization of different photothermal and imaging agents to achieve enhanced imaging and photothermal efficiencies, and understanding of nanoparticle stability via structural and surface modifications.

ASSOCIATED CONTENT

Supporting Information

The Supporting Information is available free of charge at https://pubs.acs.org/doi/10.1021/acsabm.0c00432.

Experimental details regarding synthesis, thermal analysis, optical spectra, biological images, and other supplementary results (PDF)

AUTHOR INFORMATION

Corresponding Author

Davita L. Watkins − *Department of Chemistry and Biochemistry, The University of Mississippi, University, Mississippi 38677, United States;* orcid.org/0000-0002-0943-7220; Email: dwatkins@olemiss.edu

Authors

Indika Chandrasiri − *Department of Chemistry and Biochemistry, The University of Mississippi, University, Mississippi 38677, United States*

Daniel G. Abebe − *Department of Chemistry and Biochemistry, The University of Mississippi, University, Mississippi 38677, United States*

Mahesh Loku Yaddehige − *Department of Chemistry and Biochemistry, The University of Mississippi, University, Mississippi 38677, United States*

Jon Steven Dal Williams − *Department of Chemistry and Biochemistry, The University of Mississippi, University, Mississippi 38677, United States*

Mohammad Farid Zia − *Department of Biological Sciences, The University of Southern Mississippi, Hattiesburg, Mississippi 39406, United States*

Austin Dorris − *Department of Chemistry and Biochemistry, The University of Mississippi, University, Mississippi 38677, United States*

Abigail Barker − *Department of Chemistry and Biochemistry, The University of Mississippi, University, Mississippi 38677, United States*

Briana L. Simms − *Department of Chemistry and Biochemistry, The University of Mississippi, University, Mississippi 38677, United States*

Azaziah Parker − *Department of Chemistry and Biochemistry, The University of Mississippi, University, Mississippi 38677, United States*

Bhavani Prasad Vinjamuri − *Department of Pharmaceutics and Drug Delivery, School of Pharmacy, The University of*

https://dx.doi.org/10.1021/acsabm.0c00432
ACS Appl. Bio Mater. 2020, 3, 5664−5677

Mississippi, University, Mississippi 38677, United States; orcid.org/0000-0001-5172-789X

Ngoc Le − *Department of Chemistry and Biochemistry, The University of Mississippi, University, Mississippi 38677, United States*

Jacqueline N. Gayton − *Department of Chemistry and Biochemistry, The University of Mississippi, University, Mississippi 38677, United States;* orcid.org/0000-0002-3564-1663

Mahavir Bhupal Chougule − *Department of Pharmaceutics and Drug Delivery, School of Pharmacy, The University of Mississippi, University, Mississippi 38677, United States*

Nathan I. Hammer − *Department of Chemistry and Biochemistry, The University of Mississippi, University, Mississippi 38677, United States;* orcid.org/0000-0002-6221-2709

Alex Flynt − *Department of Biological Sciences, The University of Southern Mississippi, Hattiesburg, Mississippi 39406, United States*

Jared H. Delcamp − *Department of Chemistry and Biochemistry, The University of Mississippi, University, Mississippi 38677, United States;* orcid.org/0000-0001-5313-4078

Complete contact information is available at: https://pubs.acs.org/10.1021/acsabm.0c00432

Author Contributions

The manuscript was written through the contributions of all authors. All authors have given approval to the final version of the manuscript.

Funding

NSF OIA-1757220.

Notes

The authors declare no competing financial interest.

■ ACKNOWLEDGMENTS

The authors appreciate the financial support of this work from the National Science Foundation under Grant no. NSF OIA-1757220. This work made use of the BioCryo facility of Northwestern University's NUANCE Center, which has received support from the Soft and Hybrid Nanotechnology Experimental (SHyNE) Resource (NSF ECCS-1542205); the MRSEC program (NSF DMR-1720139) at the Materials Research Center; the International Institute for Nanotechnology (IIN); and the State of Illinois, through the IIN. The MRL Shared Experimental Facilities are supported by the MRSEC Program of the NSF under Award No. DMR 1720256 and a member of the NSF-funded Materials Research Facilities Network (www.mrfn.org).

■ REFERENCES

(1) Duncan, R. Polymer conjugates as anticancer nanomedicines. *Nat. Rev. Cancer* **2006**, *6*, 688−701.

(2) Jain, R. K.; Stylianopoulos, T. Delivering nanomedicine to solid tumors. *Nat. Rev. Clin. Oncol.* **2010**, *7*, 653.

(3) Talelli, M.; Barz, M.; Rijcken, C. J.; Kiessling, F.; Hennink, W. E.; Lammers, T. Core-crosslinked polymeric micelles: principles, preparation, biomedical applications and clinical translation. *Nano Today* **2015**, *10*, 93−117.

(4) Torchilin, V. P. Targeted pharmaceutical nanocarriers for cancer therapy and imaging. *AAPS J.* **2007**, *9*, E128−E147.

(5) Wagner, V.; Dullaart, A.; Bock, A.-K.; Zweck, A. The emerging nanomedicine landscape. *Nat. Biotechnol.* **2006**, *24*, 1211−1217.

(6) Gradishar, W. J.; Tjulandin, S.; Davidson, N.; Shaw, H.; Desai, N.; Bhar, P.; Hawkins, M.; O'Shaughnessy, J. Phase III Trial of Nanoparticle Albumin-Bound Paclitaxel Compared With Polyethylated Castor Oil−Based Paclitaxel in Women With Breast Cancer. *J. Clin. Oncol.* **2005**, *23*, 7794−7803.

(7) Kloover, J. S.; den Bakker, M. A.; Gelderblom, H.; van Meerbeeck, J. P. Fatal outcome of a hypersensitivity reaction to paclitaxel: a critical review of premedication regimens. *Br. J. Cancer* **2004**, *90*, 304−305.

(8) Kabanov, A. V.; Batrakova, E. V.; Alakhov, V. Y. Pluronic block copolymers as novel polymer therapeutics for drug and gene delivery. *J. Controlled Release* **2002**, *82*, 189−212.

(9) Arifin, D. R.; Palmer, A. F. Polymersome encapsulated hemoglobin: a novel type of oxygen carrier. *Biomacromolecules* **2005**, *6*, 2172−2181.

(10) Wong, H. L.; Rauth, A. M.; Bendayan, R.; Wu, X. Y. In vivo evaluation of a new polymer-lipid hybrid nanoparticle (PLN) formulation of doxorubicin in a murine solid tumor model. *Eur. J. Pharm. Biopharm* **2007**, *65*, 300−308.

(11) Yokoyama, M. Block copolymers as drug carriers. *Crit. Rev. Ther. Drug Carrier Syst.* **1992**, *9*, 213−248.

(12) Banik, B. L.; Fattahi, P.; Brown, J. L. Polymeric nanoparticles: the future of nanomedicine. *WIREs Nanomed. Nanobiotechnol.* **2016**, *8*, 271−299.

(13) Owen, S. C.; Chan, D. P. Y.; Shoichet, M. S. Polymeric micelle stability. *Nano Today* **2012**, *7*, 53−65.

(14) Torchilin, V. P. Micellar Nanocarriers: Pharmaceutical Perspectives. *Pharm. Res.* **2007**, *24*, No. 1.

(15) Chandrasiri, I.; Abebe, D. G.; Gupta, S.; Williams, J. S. D.; Rieger, W. D.; Simms, B. L.; Yaddehige, M. L.; Noh, Y.; Payne, M. E.; Fortenberry, A. W.; Smith, A. E.; Ilavsky, J.; Grayson, S. M.; Schneider, G. J.; Watkins, D. L. Synthesis and characterization of polylactide-PAMAM "Janus-type" linear-dendritic hybrids. *J. Polym. Sci., Part A: Polym. Chem.* **2019**, *57*, 1448−1459.

(16) Gu, F. X.; Karnik, R.; Wang, A. Z.; Alexis, F.; Levy-Nissenbaum, E.; Hong, S.; Langer, R. S.; Farokhzad, O. C. Targeted nanoparticles for cancer therapy. *Nano Today* **2007**, *2*, 14−21.

(17) Lee, E. S.; Shin, J. M.; Son, S.; Ko, H.; Um, W.; Song, S. H.; Lee, J. A.; Park, J. H. Recent Advances in Polymeric Nanomedicines for Cancer Immunotherapy. *Adv. Healthcare Mater.* **2019**, *8*, No. 1801320.

(18) Zhang, L.; Gu, F.; Chan, J.; Wang, A.; Langer, R.; Farokhzad, O. Nanoparticles in Medicine: Therapeutic Applications and Developments. *Clin. Pharmacol. Ther.* **2008**, *83*, 761−769.

(19) Bor, G.; Azmi, I. D. M.; Yaghmur, A. Nanomedicines for cancer therapy: current status, challenges and future prospects. *Ther. Delivery* **2019**, *10*, 113−132.

(20) Calzoni, E.; Cesaretti, A.; Polchi, A.; Di Michele, A.; Tancini, B.; Emiliani, C. Biocompatible Polymer Nanoparticles for Drug Delivery Applications in Cancer and Neurodegenerative Disorder Therapies. *J. Funct. Biomater.* **2019**, *10*, No. 4.

(21) Farokhzad, O. C.; Langer, R. Nanomedicine: Developing smarter therapeutic and diagnostic modalities. *Adv. Drug Delivery Rev.* **2006**, *58*, 1456−1459.

(22) Liu, G.-Y.; Liu, X.-S.; Wang, S.-S.; Chen, C.-J.; Ji, J. Biomimetic Polymersomes as Carriers for Hydrophilic Quantum Dots. *Langmuir* **2012**, *28*, 557−562.

(23) Liao, J.; Li, W.; Peng, J.; Yang, Q.; Li, H.; Wei, Y.; Zhang, X.; Qian, Z. Combined cancer photothermal-chemotherapy based on doxorubicin/gold nanorod-loaded polymersomes. *Theranostics* **2015**, *5*, 345−356.

(24) Mohammadi, M.; Ramezani, M.; Abnous, K.; Alibolandi, M. Biocompatible polymersomes-based cancer theranostics: Towards multifunctional nanomedicine. *Int. J. Pharm.* **2017**, *519*, 287−303.

(25) Opsteen, J. A.; Cornelissen, J. J. L. M.; van Hest, J. C. M. Block copolymer vesicles. *Pure Appl. Chem.* **2004**, *76*, 1309.

(26) Cho, H. K.; Cheong, I. W.; Lee, J. M.; Kim, J. H. Polymeric nanoparticles, micelles and polymersomes from amphiphilic block copolymer. *Korean J. Chem. Eng.* **2010**, *27*, 731−740.

(27) Fedeli, E.; Lancelot, A.; Dominguez, J. M.; Serrano, J. L.; Calvo, P.; Sierra, T. Self-Assembling Hybrid Linear-Dendritic Block Copolymers: The Design of Nano-Carriers for Lipophilic Antitumoral Drugs. *Nanomaterials* **2019**, *9*, No. 161.
(28) Kim, Y. S.; Gulfam, M.; Lowe, T. L. Thermoresponsive-co-Biodegradable Linear−Dendritic Nanoparticles for Sustained Release of Nerve Growth Factor To Promote Neurite Outgrowth. *Mol. Pharm.* **2018**, *15*, 1467−1475.
(29) Gayton, J.; Autry, S. A.; Meador, W.; Parkin, S. R.; Hill, G. A.; Hammer, N. I.; Delcamp, J. H. Indolizine-Cyanine Dyes: Near Infrared Emissive Cyanine Dyes with Increased Stokes Shifts. *J. Org. Chem.* **2019**, *84*, 687−697.
(30) Hornig, S.; Heinze, T.; Becer, C. R.; Schubert, U. S. Synthetic polymeric nanoparticles by nanoprecipitation. *J. Mater. Chem.* **2009**, *19*, 3838−3840.
(31) Rangelov, S.; Pispas, A. *Polymer and Polymer-Hybrid Nanoparticles: From Synthesis to Biomedical Applications*; CRC Press, 2013.
(32) Buwalda, S.; Al Samad, A.; El Jundi, A.; Bethry, A.; Bakkour, Y.; Coudane, J.; Nottelet, B. Stabilization of poly(ethylene glycol)-poly(epsilon-caprolactone) star block copolymer micelles via aromatic groups for improved drug delivery properties. *J. Colloid Interface Sci.* **2018**, *514*, 468−478.
(33) Esfand, R.; Tomalia, D. A. Poly(amidoamine) (PAMAM) dendrimers: from biomimicry to drug delivery and biomedical applications. *Drug Discovery Today* **2001**, *6*, 427−436.
(34) Fréchet, J. M. J.; Hawker, C. J.; Gitsov, I.; Leon, J. W. Dendrimers and Hyperbranched Polymers: Two Families of Three-Dimensional Macromolecules with Similar but Clearly Distinct Properties. *J. Macromol. Sci., Part A: Pure Appl.Chem.* **1996**, *33*, 1399−1425.
(35) Li, Z.; Tan, B. H. Towards the development of polycaprolactone based amphiphilic block copolymers: molecular design, self-assembly and biomedical applications. *Mater. Sci. Eng., C* **2014**, *45*, 620−634.
(36) Perveen, R.; Nasar, A. Multiwalled Carbon Nanotube-based Nanocomposites for Artificial Bone Grafting. *Applications of Nanocomposite Materials in Orthopedics*; Elsevier, 2019; pp 111−126.
(37) Hua, C.; Dong, C.-M.; Wei, Y. Versatile strategy for the synthesis of dendronlike polypeptide/linear poly (ε-caprolactone) block copolymers via click chemistry. *Biomacromolecules* **2009**, *10*, 1140−1148.
(38) Dong, C.-M.; Liu, G. Linear−dendritic biodegradable block copolymers: from synthesis to application in bionanotechnology. *Polym. Chem.* **2013**, *4*, 46−52.
(39) Abebe, D. G.; Kandil, R.; Kraus, T.; Elsayed, M.; Merkel, O. M.; Fujiwara, T. Three-layered biodegradable micelles prepared by two-step self-assembly of PLA-PEI-PLA and PLA-PEG-PLA triblock copolymers as efficient gene delivery system. *Macromol. Biosci.* **2015**, *15*, 698−711.
(40) Remant Bahadur, K. C.; Bhattarai, S. R.; Aryal, S.; Khil, M. S.; Dharmaraj, N.; Kim, H. Y. Novel amphiphilic triblock copolymer based on PPDO, PCL, and PEG: Synthesis, characterization, and aqueous dispersion. *Colloids Surf., A* **2007**, *292*, 69−78.
(41) Bhattarai, N.; Kim, H. Y.; Lee, D. R. Thermogravimetric study of copolymers derived from p-dioxanone, L-lactide and poly (ethylene glycol). *Polym. Degrad. Stab.* **2002**, *78*, 423−433.
(42) Drumond, W. S.; Mothé, C. G.; Wang, S. H. Quantitative analysis of biodegradable amphiphilic poly(L-lactide)-block-poly-(ethyleneglycol)-blockpoly(L-lactide) by using TG, FTIR and NMR. *J. Therm. Anal. Calorim.* **2006**, *85*, 173−177.
(43) Adedeji, A.; Lyu, S.; Macosko, C. W. Block Copolymers in Homopolymer Blends: Interface vs Micelles. *Macromolecules* **2001**, *34*, 8663−8668.
(44) Martínez Rivas, C. J.; Tarhini, M.; Badri, W.; Miladi, K.; Greige-Gerges, H.; Nazari, Q. A.; Galindo Rodríguez, S. A.; Román, R. Á.; Fessi, H.; Elaissari, A. Nanoprecipitation process: From encapsulation to drug delivery. *Int. J. Pharm.* **2017**, *532*, 66−81.
(45) Cerritelli, S.; Fontana, A.; Velluto, D.; Adrian, M.; Dubochet, J.; De Maria, P.; Hubbell, J. A. Thermodynamic and kinetic effects in the aggregation behavior of a poly (ethylene glycol-b-propylene sulfide-b-ethylene glycol) ABA triblock copolymer. *Macromolecules* **2005**, *38*, 7845−7851.
(46) Blanazs, A.; Armes, S. P.; Ryan, A. J. Self-Assembled Block Copolymer Aggregates: From Micelles to Vesicles and their Biological Applications. *Macromol. Rapid Commun.* **2009**, *30*, 267−277.
(47) Zhang, S.; Sun, H.-J.; Hughes, A. D.; Moussodia, R.-O.; Bertin, A.; Chen, Y.; Pochan, D. J.; Heiney, P. A.; Klein, M. L.; Percec, V. Self-assembly of amphiphilic Janus dendrimers into uniform onion-like dendrimersomes with predictable size and number of bilayers. *Proc. Natl. Acad. Sci. U.S.A.* **2014**, *111*, 9058−9063.
(48) Zhao, J.; Nagao, S.; Odegard, G. M.; Zhang, Z.; Kristiansen, H.; He, J. Size-dependent mechanical behavior of nanoscale polymer particles through coarse-grained molecular dynamics simulation. *Nanoscale Res. Lett.* **2013**, *8*, No. 541.
(49) Yao, Y.; Wei, Y.; Chen, S. Size effect of the surface energy density of nanoparticles. *Surf. Sci.* **2015**, *636*, 19−24.
(50) Singer, A.; Barakat, Z.; Mohapatra, S.; Mohapatra, S. S. Nanoscale Drug-Delivery Systems: In Vitro and In Vivo Characterization. *Nanocarriers for Drug Delivery*; Elsevier, 2019; pp 395−419.
(51) Mai, Y.; Eisenberg, A. Self-assembly of block copolymers. *Chem. Soc. Rev.* **2012**, *41*, 5969−5985.
(52) Israelachvili, J. N. *Intermolecular and Surface Forces*; Academic Press, 2015.
(53) Israelachvili, J. N.; Mitchell, D. J.; Ninham, B. W. Theory of self-assembly of lipid bilayers and vesicles. *Biochim. Biophys. Acta, Biomembr.* **1977**, *470*, 185−201.
(54) Israelachvili, J.; Mitchell, D.; Ninham, B. *J. Chem. Soc., Faraday Trans. 2* **1976**, *72*, 1525−1568.
(55) Israelachvili, J. *Intermolecular and Surface Forces*, 2nd ed.; Academic Press: London, 1992.
(56) Fröhlich, E. The role of surface charge in cellular uptake and cytotoxicity of medical nanoparticles. *Int. J. Nanomed.* **2012**, *7*, 5577.
(57) Blanco, E.; Shen, H.; Ferrari, M. Principles of nanoparticle design for overcoming biological barriers to drug delivery. *Nat. Biotechnol.* **2015**, *33*, 941−951.
(58) Shao, X. R.; Wei, X. Q.; Song, X.; Hao, L. Y.; Cai, X. X.; Zhang, Z. R.; Peng, Q.; Lin, Y. F. Independent effect of polymeric nanoparticle zeta potential/surface charge, on their cytotoxicity and affinity to cells. *Cell Proliferation* **2015**, *48*, 465−474.
(59) He, C.; Hu, Y.; Yin, L.; Tang, C.; Yin, C. Effects of particle size and surface charge on cellular uptake and biodistribution of polymeric nanoparticles. *Biomaterials* **2010**, *31*, 3657−3666.
(60) Khan, N.; Brettmann, B. Intermolecular Interactions in Polyelectrolyte and Surfactant Complexes in Solution. *Polymers* **2018**, *11*, No. 51.
(61) Dutta, P.; Shrivastava, S.; Dey, J. Amphiphilic polymer nanoparticles: characterization and assessment as new drug carriers. *Macromol. Biosci.* **2009**, *9*, 1116−1126.
(62) Dumitriu, S.; Popa, V. *Polymeric Biomaterials: Structure and Function*; CRC Press, 2013; Vol. *1*.
(63) Kataoka, K.; Harada, A.; Nagasaki, Y. Block copolymer micelles for drug delivery: design, characterization and biological significance. *Adv. Drug Delivery Rev.* **2012**, *64*, 37−48.
(64) Sharma, R.; Gescher, A.; Steward, W. Curcumin: the story so far. *Eur. J. Cancer* **2005**, *41*, 1955−1968.
(65) Sanidad, K. Z.; Sukamtoh, E.; Xiao, H.; McClements, D. J.; Zhang, G. Curcumin: recent advances in the development of strategies to improve oral bioavailability. *Annu. Rev. Food Sci. Technol.* **2019**, *10*, 597−617.
(66) Gao, Z.; Eisenberg, A. A model of micellization for block copolymers in solutions. *Macromolecules* **1993**, *26*, 7353−7360.
(67) Jones, M.; Leroux, J. Polymeric micelles - a new generation of colloidal drug carriers. *Eur. J. Pharm. Biopharm.* **1999**, *48*, 101−111.
(68) Shi, C.; Wu, J. B.; Pan, D. Review on near-infrared heptamethine cyanine dyes as theranostic agents for tumor imaging, targeting, and photodynamic therapy. *J. Biomed. Opt.* **2016**, *21*, No. 050901.

https://dx.doi.org/10.1021/acsabm.0c00432
ACS Appl. Bio Mater. 2020, 3, 5664−5677

(69) Licha, K.; Riefke, B.; Ntziachristos, V.; Becker, A.; Chance, B.; Semmler, W. Hydrophilic Cyanine Dyes as Contrast Agents for Near-infrared Tumor Imaging: Synthesis, Photophysical Properties and Spectroscopic In vivo Characterization. *Photochem. Photobiol.* **2000**, *72*, 392−398.
(70) Luo, S.; Zhang, E.; Su, Y.; Cheng, T.; Shi, C. A review of NIR dyes in cancer targeting and imaging. *Biomaterials* **2011**, *32*, 7127−7138.
(71) Delcamp, J. H.; Shi, Y.; Yum, J. H.; Sajoto, T.; Dell'Orto, E.; Barlow, S.; Nazeeruddin, M. K.; Marder, S. R.; Grätzel, M. The Role of π Bridges in High-Efficiency DSCs Based on Unsymmetrical Squaraines. *Chem. - Eur. J.* **2013**, *19*, 1819−1827.
(72) Gayton, J. N.; Autry, S.; Fortenberry, R. C.; Hammer, N. I.; Delcamp, J. H. Counter Anion Effect on the Photophysical Properties of Emissive Indolizine-Cyanine Dyes in Solution and Solid State. *Molecules* **2018**, *23*, No. 3051.
(73) Meador, W. E.; Autry, S. A.; Bessetti, R. N.; Gayton, J. N.; Flynt, A. S.; Hammer, N. I.; Delcamp, J. H. Water-Soluble NIR Absorbing and Emitting Indolizine Cyanine and Indolizine Squaraine Dyes for Biological Imaging. *J. Org. Chem.* **2020**, *85*, 4089−4095.
(74) Sulas, D. B.; London, A. E.; Huang, L.; Xu, L.; Wu, Z.; Ng, T. N.; Wong, B. M.; Schlenker, C. W.; Azoulay, J. D.; Sfeir, M. Y. Preferential Charge Generation at Aggregate Sites in Narrow Band Gap Infrared Photoresponsive Polymer Semiconductors. *Adv. Opt. Mater.* **2018**, *6*, No. 1701138.
(75) Jain, A. K.; Thanki, K.; Jain, S. Co-encapsulation of Tamoxifen and Quercetin in Polymeric Nanoparticles: Implications on Oral Bioavailability, Antitumor Efficacy, and Drug-Induced Toxicity. *Mol. Pharm.* **2013**, *10*, 3459−3474.
(76) Deng, X.; Liang, Y.; Peng, X.; Su, T.; Luo, S.; Cao, J.; Gu, Z.; He, B. A facile strategy to generate polymeric nanoparticles for synergistic chemo-photodynamic therapy. *Chem. Commun.* **2015**, *51*, 4271−4274.
(77) Buwalda, S.; Al Samad, A.; El Jundi, A.; Bethry, A.; Bakkour, Y.; Coudane, J.; Nottelet, B. Stabilization of poly(ethylene glycol)-poly(ε-caprolactone) star block copolymer micelles via aromatic groups for improved drug delivery properties. *J. Colloid Interface Sci.* **2018**, *514*, 468−478.
(78) Kim, H. S.; Wainer, I. W. Simultaneous analysis of liposomal doxorubicin and doxorubicin using capillary electrophoresis and laser induced fluorescence. *J. Pharm. Biomed. Anal.* **2010**, *52*, 372−376.
(79) Suk, J. S.; Xu, Q.; Kim, N.; Hanes, J.; Ensign, L. M. PEGylation as a strategy for improving nanoparticle-based drug and gene delivery. *Adv. Drug Delivery Rev.* **2016**, *99*, 28−51.
(80) Fonte, P.; Reis, S.; Sarmento, B. Facts and evidences on the lyophilization of polymeric nanoparticles for drug delivery. *J. Controlled Release* **2016**, *225*, 75−86.
(81) Elwell, C.; Engel, J. N. *Drosophila melanogaster* S2 cells: a model system to study Chlamydia interaction with host cells. *Cell. Microbiol.* **2005**, *7*, 725−739.
(82) Romine, M. L.; Li, M.; Liu, K. J.; Patel, S. K.; Nelson, J. G.; Shen, P.; Cai, H. N. A Cell Density-dependent Reporter in the Drosophila S2 cells. *Sci. Rep.* **2019**, *9*, No. 11868.
(83) Moore, T. L.; Rodriguez-Lorenzo, L.; Hirsch, V.; Balog, S.; Urban, D.; Jud, C.; Rothen-Rutishauser, B.; Lattuada, M.; Petri-Fink, A. Nanoparticle colloidal stability in cell culture media and impact on cellular interactions. *Chem. Soc. Rev.* **2015**, *44*, 6287−6305.
(84) Shi, H.; He, X.; Yuan, Y.; Wang, K.; Liu, D. Nanoparticle-based biocompatible and long-life marker for lysosome labeling and tracking. *Anal. Chem.* **2010**, *82*, 2213−2220.
(85) Griffiths, G.; Hoflack, B.; Simons, K.; Mellman, I.; Kornfeld, S. The mannose 6-phosphate receptor and the biogenesis of lysosomes. *Cell* **1988**, *52*, 329−341.
(86) Duong, T.; Li, X.; Yang, B.; Schumann, C.; Albarqi, H. A.; Taratula, O.; Taratula, O. Phototheranostic nanoplatform based on a single cyanine dye for image-guided combinatorial phototherapy. *Nanomedicine* **2017**, *13*, 955−963.
(87) Smith, B. R.; Gambhir, S. S. Nanomaterials for In Vivo Imaging. *Chem. Rev.* **2017**, *117*, 901−986.
(88) Cho, E. J.; Holback, H.; Liu, K. C.; Abouelmagd, S. A.; Park, J.; Yeo, Y. Nanoparticle characterization: state of the art, challenges, and emerging technologies. *Mol. Pharm.* **2013**, *10*, 2093−2110.
(89) Lu, Y.; Zhang, E.; Yang, J.; Cao, Z. Strategies to improve micelle stability for drug delivery. *Nano Res.* **2018**, *11*, 4985−4998.
(90) Nelemans, L. C.; Gurevich, L. Drug Delivery with Polymeric Nanocarriers—Cellular Uptake Mechanisms. *Materials* **2020**, *13*, No. 366.
(91) Ulbrich, K.; Hola, K.; Subr, V.; Bakandritsos, A.; Tucek, J.; Zboril, R. Targeted drug delivery with polymers and magnetic nanoparticles: covalent and noncovalent approaches, release control, and clinical studies. *Chem. Rev.* **2016**, *116*, 5338−5431.

https://dx.doi.org/10.1021/acsabm.0c00432
ACS Appl. Bio Mater. 2020, 3, 5664−5677